





## HIGH-RESOLUTION RAY TRACING MIGRATION

Danian Steinkirch de Oliveira <sup>1</sup>, Paulo Eduardo Miranda Cunha <sup>2</sup>,  
Luiz Gallisa Guimarães <sup>3</sup>, and Andre Fabiano Steklain Lisboa <sup>4</sup>

**ABSTRACT.** We present a seismic migration algorithm that calculates travel times and amplitudes based on the paraxial extrapolation of the dynamic ray tracing. We use a target-oriented approach with automatic selection of migration parameters and seismic traces that will compose the image. By associating the ray parameter (slowness vector) with the amplitudes of the seismic data, we reach a new form of migration amplitude conditioner that acts as a filter and may increase the resolution of reflectors and faults. On the other hand, when using the seismic amplitudes as weights, we can estimate the slowness vectors associated with the true seismic reflectors in depth. We apply this method to the synthetic seismic data of the Marmousi velocity model. When comparing the migrated seismic section to the true interval velocity model, we can see a precise matching of the geological features in a high-resolution pattern.

**Keywords:** seismic migration, target-orientation, dynamic ray tracing, paraxial amplitude extrapolation.

**RESUMO.** Apresentamos um algoritmo de migração sísmica que calcula tempos de trânsito e amplitudes com base na extrapolação paraxial do traçado dinâmico de raios. Utilizamos uma abordagem orientada a alvos com seleção automática dos parâmetros de migração e dos traços sísmicos que irão compor a imagem. Ao associar o parâmetro de raio (vetor de vagarosidade) às amplitudes dos dados sísmicos, chegamos a uma nova forma de condicionador de amplitudes de migração que atua como filtro e pode aumentar a resolução de refletores e falhas. Por outro lado, ao usar as amplitudes sísmicas como pesos, podemos estimar os vetores de vagarosidade associados aos verdadeiros refletores sísmicos em profundidade. Aplicamos este método aos dados sísmicos sintéticos do modelo de velocidade de Marmousi. Ao comparar a seção sísmica migrada com o modelo de velocidades intervalar verdadeiro, podemos ver uma correspondência precisa das feições geológicas em um padrão de alta resolução.

**Palavras-chave:** migração sísmica, orientação ao alvo, traçado dinâmico de raios, extrapolação paraxial de amplitude.

Corresponding author: Danian Steinkirch de Oliveira

<sup>1</sup>PETROBRAS, Petrobras Research Center – CENPES, 21941-915 Rio de Janeiro, RJ Brazil – E-mails: danian@petrobras.com.br, danian.oliveira@gmail.com

<sup>2</sup>PETROBRAS, Petrobras Research Center – CENPES (retired), Rio de Janeiro, RJ Brazil – Email: pemcunha@gmail.com

<sup>3</sup>Universidade Federal do Rio de Janeiro – UFRJ, COPPE, Oceanic Engineering, 21945-970 Rio de Janeiro, RJ, Brazil – Email: lula@if.ufrj.br

<sup>4</sup>Universidade Tecnológica Federal do Paraná – UTFPR, Mathematics Department, 80230-901 Curitiba, PR, Brazil – Email: steklain@utfpr.edu.br

## INTRODUCTION

Seismic migration aims to produce an image of the subsurface structures using wavefield extrapolation methods (Biondi, 2006). Nowadays, several migration techniques are available for the industry such as Kirchhoff (Schleicher *et al.*, 1993), Gaussian beams (Hill, 2001; Gray, 2005; Popov *et al.*, 2010), and Reverse Time Migration (Baysal *et al.*, 1983).

The first ones are asymptotic high-frequency methods that employ dynamic ray tracing to compute, explicitly or implicitly, the travel times and amplitudes of the reflectors, and have a good balance between accuracy, flexibility and speed (Bleistein *et al.*, 2000). The Reverse Time Migration (RTM) is expected to have higher accuracy as it employs the complete wave equation, but it is slower when results with high-frequency content are required (Zhou *et al.*, 2018).

The true amplitude Kirchhoff operator for depth migration performs a weighted sum of the wavefield along a diffraction curve (Schleicher *et al.*, 1993). The weights are obtained by the stationary phase technique (Bleistein, 1984). In this work, we present an algorithm for Kirchhoff migration by paraxial beams in a target-oriented approach.

While seismic migration algorithms are well established, in the last two decades, obtaining a model of rock properties in subsurface, such as the wave propagation velocity, has become the main goal of reflection seismic imaging (Virieux and Operto, 2009). In large volumes of data, the elapsed time needed for modeling and inversion by techniques such as Full Waveform Inversion (FWI) still has great importance. To reduce this time, it is possible to use seismic tomography as an alternative for velocity estimation (Woodward *et al.*, 2008). The tomography can be performed with dynamic ray tracing, which is well known for rapidly modeling of the wavefield amplitudes and travel times.

However, in places where there are great contrasts of seismic velocities, ray tracing has limitations (Operto *et al.*, 2000) and must be replaced by some other wave equation solution methods based on finite differences, finite elements, or pseudo-spectral approaches (Carcione *et al.*, 2002). Possibly, a combination of dynamic ray tracing with these other wave equation solution methods, similar to the ones presented by Sava and Fomel (2005) and Shragge (2008); Shragge and Akerberg (2010), may hold the next stages of seismic imaging.

Ray methods are suitable for subsurface target-oriented imaging and are less costly compared to two-way wave-equation-based migration, but for complex geological settings the two-way wave equation is generally used for wavefield extrapolation (Rocha *et al.*, 2018). Virieux and Farra (1991) have already addressed the issue of imaging in complex media using ray tracing. In this work, we will show that even in geological conditions of high structural complexity, such as the 2D synthetic model Marmousi (Versteeg, 1994), dy-

namic ray tracing operators can achieve a good result in imaging and can reach a very satisfactory resolution. We assume that this degree of resolution was achieved due to the accuracy of the dynamic ray tracing associated with the sensitivity of paraxial extrapolation and the way of calculating paraxial amplitudes, as described in Cunha *et al.* (2005).

In addition, we implement a target-oriented strategy that selects the traces that most contribute to the imaged point and vector amplitudes, which significantly increases the resolution, both in seismic horizons and faults. In the next sections, we explain in more detail the theoretical development of our model and analyze the main results.

## THE DYNAMIC RAY TRACING

The seismic ray method is based on the approximate high-frequency solution of the elastodynamic equation. It leads to the decomposition of the wavefield into independent contributions called elementary waves, which propagate along the rays (Cerveny, 2001). The ray tracing method has been described in detail by several authors such as Cerveny (2001), Bleistein *et al.* (2000) and Chapman (2004).

The propagating field  $u(\mathbf{x})$  in the point  $\mathbf{x}$ , due to point source  $F(w)$  at  $\mathbf{x}_s$ , can be represented by the integral operator,

$$u(\mathbf{x}, \mathbf{x}_s, t) = \frac{\mathcal{R}e}{\pi} \int_{\omega=0}^{+\infty} F(\mathbf{x}_s, \omega) G(\mathbf{x}, \mathbf{x}_s, \omega) e^{-i\omega t} d\omega. \quad (1)$$

The asymptotic approximation of the 2D Green's function for a non-homogeneous media can be represented by

$$G(\mathbf{x}, \omega) = \frac{\Psi_0(\omega)}{\sqrt{\mathcal{J}(\mathbf{x})}} e^{i\omega\tau(\mathbf{x})}, \quad (2)$$

where the Jacobean  $\mathcal{J}(\mathbf{x})$  is denoted by

$$\mathcal{J}(\mathbf{x}) = \det \begin{bmatrix} \frac{\partial \mathbf{x}}{\partial \sigma} & \frac{\partial \mathbf{x}}{\partial \alpha} \end{bmatrix} = \left| \left[ \frac{\partial \mathbf{x}}{\partial \gamma} \right] \right| = |[\mathbf{p}_\sigma, \mathbf{p}_\alpha]|. \quad (3)$$

The 2D global ray coordinates are determined by  $\sigma$ , which represents the direction of the wavefront, and  $\alpha$ , the shooting angle.  $\gamma(\sigma, \alpha)$  can be understood as the direction towards the central ray. The parameter  $\sigma$  is denoted by

$$\partial\sigma = c\partial s = c^2\partial\tau, \quad (4)$$

where  $\partial\tau$  is the time interval,  $\partial s$  is the arc length of the ray path, and  $c(\mathbf{x}(\sigma))$  is the velocity field at the point  $\mathbf{x}(\sigma)$ .

The function  $\Psi_0(\omega)$  in Eq. 5 is a calibration factor of the initial amplitude, defined by Popov (2002), for the asymptotic approximation of the 2D Green function, given by

$$\Psi_0(\omega) = \frac{e^{i\frac{\pi}{4}}}{2\sqrt{2\pi\omega}}. \quad (5)$$

The dynamic ray tracing algorithm is based on the solu-

tion of the system of kinematic,

$$\frac{d}{d\sigma} \begin{bmatrix} \mathbf{x}(\sigma) \\ \mathbf{p}(\sigma) \end{bmatrix} = J \begin{bmatrix} \nabla_{\mathbf{x}} \left( \frac{1}{2c^2(\mathbf{x}(\sigma))} \right) \\ \mathbf{p} \end{bmatrix} \quad (6)$$

and dynamic

$$\frac{d}{d\sigma} \begin{bmatrix} \frac{\partial \mathbf{x}}{\partial \gamma}(\sigma) \\ \frac{\partial \mathbf{p}}{\partial \gamma}(\sigma) \end{bmatrix} = J \begin{bmatrix} -\nabla_{\mathbf{x}} \nabla_{\mathbf{x}} \left( \frac{1}{2c^2(\mathbf{x}(\sigma))} \right) & \mathbf{0} \\ \mathbf{0} & \mathbf{1} \end{bmatrix} \begin{bmatrix} \frac{\partial \mathbf{x}}{\partial \gamma}(\sigma) \\ \frac{\partial \mathbf{p}}{\partial \gamma}(\sigma) \end{bmatrix} \quad (7)$$

differential equations, where

$$J = \begin{bmatrix} \mathbf{0} & \mathbf{1} \\ -\mathbf{1} & \mathbf{0} \end{bmatrix}. \quad (8)$$

The first system of equations (6) provides the trajectory  $\mathbf{x}(\sigma)$  and the slowness  $\mathbf{p}(\sigma)$  of the rays (Cunha, 2009). The system of differential equations in (7) propagates the paraxial information that will later be used in the expansion of travel times and asymptotic amplitudes.

### Travel time and asymptotic amplitude extrapolation

The extrapolation of the travel times  $\tau(\mathbf{x}_0)$  from the central ray to the travel times  $\tau(\mathbf{x})$  in the points of the grid in the vicinity of the ray (Fig. 1) is made through the expansion of the Taylor series. The paraxial information  $\mathbf{p}(\mathbf{x}_0)$  and  $M_0$  in Eq.(9), provided by the solution of the extended system of differential equations of the ray tracing propagator, allow us to expand the travel times up to the second-order term of the Taylor series (Cunha et al., 2005), represented by

$$\tau(\mathbf{x}) = \tau(\mathbf{x}_0) + \mathbf{p}(\mathbf{x}_0) \cdot \delta \mathbf{x} + \frac{1}{2} \langle \langle M_0, \delta \mathbf{x} \rangle, \delta \mathbf{x} \rangle + \mathcal{O}(|\delta \mathbf{x}|^3), \quad (9)$$

where  $\langle \cdot, \cdot \rangle$  represents the dot product and matrix  $M_0$  is the second order contribution to the Taylor series, given by

$$M_0 = \left[ \frac{\partial \mathbf{p}}{\partial \gamma} \right] \left[ \frac{\partial \mathbf{x}}{\partial \gamma} \right]^{-1} \Bigg|_{\mathbf{x}_0} \quad (10)$$

and

$$\delta \mathbf{x} = \mathbf{x} - \mathbf{x}_0 \quad \left. \frac{\partial \tau(\mathbf{x})}{\partial \mathbf{x}} \right|_{\mathbf{x}_0} = \mathbf{p}(\mathbf{x}_0). \quad (11)$$

The slowness  $\mathbf{p}(\mathbf{x}_0)$  and ray coordinates  $\mathbf{x}_0$  are given by the kinematic system (6). The second derivatives  $M_0$  are obtained by the dynamic system (7).

The geometrical spreading  $\mathcal{J}(\mathbf{x})$ , at a point on the grid, close to the ray, will be determined by a Taylor series expansion up to the first-order term from the Jacobean  $\mathcal{J}(\mathbf{x}_0)$  at the point  $\mathbf{x}_0$  of the ray, obtained from the propagator in Eq. 6, given by

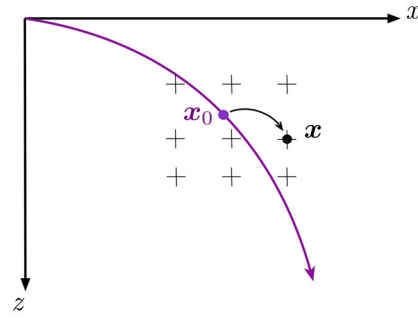


Figure 1. Paraxial extrapolation scheme from a point  $\mathbf{x}_0$ , belonging to the central ray, to a point  $\mathbf{x}$  of the model grid in the vicinity of the central ray.

$$\mathcal{J}(\mathbf{x}) = \mathcal{J}(\mathbf{x}_0) + \left. \frac{\partial \mathcal{J}(\mathbf{x})}{\partial \mathbf{x}} \right|_{\mathbf{x}_0} \cdot \delta \mathbf{x} + \mathcal{O}(\|\mathbf{x} - \mathbf{x}_0\|^2) \quad (12)$$

More details on the calculation of paraxial amplitudes can be seen in Appendix C.

### TARGET-ORIENTED APPROACH

In our method, the seismic data migration is performed in the shot domain using ray tracing as a tool for modeling the times and amplitudes of the propagated wave field. The management of travel time and amplitude maps is very similar to that presented by Thierry et al. (1999), regarding storage and access to the computer memory. The algorithm flexibility allows the migration of small areas of interest without the need of migrating the entire seismic section or volume. We call this a target-oriented approach, similar to Koren et al. (2002), but with some modifications that we will show next in more detail.

Within the acquisition region, the target area to be imaged is determined as shown in Figure 2. The target area is then separated into sub-targets. This separation is done automatically by the program, according to the input parameter width and depth (in the 2D case) that define the size of the sub-target in the  $x$  and  $z$  directions (both in meters), respectively.

The number and location of the sub-target centers are managed by the program, which will always extend the border of the area of interest. The size in the  $x$ -direction should not be too large in order to avoid low illumination due to the turning rays. Once the sub-targets are determined, the target-oriented approach modeling process begins. The target-oriented approach has two main steps, upward modeling (first step) and downward modeling (second step), as shown in Figure 3. The general scheme of the migration algorithm is also shown in Appendix A. In the first step the sub-target centers are calculated, and the modeling part begins by shooting rays upwards from the sub-target center towards the acquisition surface  $\Sigma_0$  (Fig. 4), where the ray param-

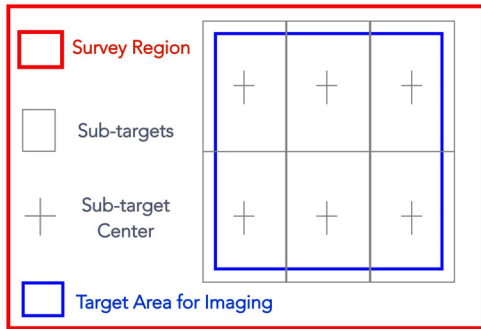


Figure 2. The region of interest or region of seismic acquisition is in red. The target to be imaged (blue) can present a size of a few hundred meters or even the size of the acquisition region. The subdivisions of the target or sub-targets, with their respective centers, are in black. The sub-targets present a size of hundreds of meters to a few kilometers. The width of the sub-target should not be too large to avoid illumination loss due to the low coverage of the rays.

ters, such as time, amplitudes and the slowness vector (Cerveny, 2001), are registered.

This step is done only once for each target. Surface stations (shot and receiver) that have non-zero amplitudes will be used in the sub-target imaging. This procedure defines the migration aperture for the target. The automatic estimation of the migration aperture is also the subject of investigation by authors like Koren *et al.* (2002) and Klovov and Fomel (2013). The migration aperture is usually defined by limiting the migration operator, through the angle or offset parameters (Russell, 1998). In this work, the automatic estimation of the migration aperture is directly related to the velocity model and the target illumination.

In the second step the amplitudes and travel times for each point in the sub-target window are calculated. From the stations in the acquisition surface, rays are traced towards the sub-target center (Fig. 5). The slowness vectors calculated in the first step are used to define the angular variation of the rays, shot from a given station. This procedure can be considered equivalent to the migration angle parameter, in a conventional PSDM (Pre-Stack Depth Migration) algorithm (e.g., Hertweck *et al.* (2003)).

The dynamic ray tracing performed in the second step for one station (shown in Fig. 6) is repeated for all stations with non-zero amplitude values in the surface acquisition (estimated in step one). The paraxial extrapolation distance, from the central ray, is controlled by parameters that depend on the velocity field and the dominant frequency and are limited by the size of the sub-target. The amplitude and travel time maps, corresponding to the paraxial extrapolation from the central ray, are represented in Figures 7a and 7b, respectively.

We apply a Gaussian smoothing operator with a length of 200 meters to the Marmousi synthetic velocity model for modeling the travel times and amplitudes in these steps. This operator size is mentioned by other authors like Operto *et al.* (2000) and Gajewski *et al.* (2002). We tried to smooth the velocity model so that the ray would not suffer too much perturbation in its trajectories and, at the same time, guarantee fidelity in the modeled travel times.

## RAY TRACING MIGRATION

Once the region of the sub-target is established, the program calculates the Kirchhoff integral for each shot using the travel time and amplitude maps obtained from the information of the dynamic ray tracing by paraxial beams. The depth imaging is performed by migrating the seismic data, in the form of the seismograms  $S(\mathbf{x}_{s_j}, \mathbf{x}_r, t)$  in the shot domain, where  $\mathbf{x}_{s_j}$  is the coordinate of the shot station on the surface and  $\mathbf{x}_r$  represents the set of receivers of a particular shot group  $s_j$ . The same operator (1), that propagates the field, migrates the seismic data, performing the backpropagation of seismic traces. Let

$$u(\mathbf{x}, \mathbf{x}_{s_j}, t) = \frac{\mathcal{R}e}{\pi} \int_{\omega=0}^{+\infty} d\omega e^{-i\omega t} \int_{\mathbf{x}_{r_i} \in \Sigma_0} S(\mathbf{x}_{s_j}, \mathbf{x}_{r_i}, \omega) \frac{\partial}{\partial z(\mathbf{x}_{r_i})} G(\mathbf{x}, \mathbf{x}_{s_j}, \mathbf{x}_{r_i}, \omega) d\mathbf{x}_{r_i} \quad (13)$$

be the contribution of the source  $\mathbf{x}_{s_j}$  to the field at the diffracting point  $\mathbf{x}$ , in subsurface, measured in the  $\mathbf{x}_{r_i}$  receiver stations located on the seismic acquisition surface  $\Sigma_0$ . The seismic trace  $S(\mathbf{x}_{s_j}, \mathbf{x}_{r_i}, \omega)$  is related to the source and receiver station pair in the frequency domain.

Using the Eq. 30 to replace the Green's function derivative of Equation 13, we can write the operator as

$$u(\mathbf{x}, \mathbf{x}_{s_j}, t) = \frac{\mathcal{R}e}{\pi} \int_{\omega=0}^{+\infty} i\omega \Psi_0(\omega) S(\mathbf{x}_{s_j}, \mathbf{x}_{r_i}, \omega) e^{-i\omega t} d\omega \int_{\mathbf{x}_{r_i} \in \mathcal{S}_0} \mathcal{A}(\mathbf{x}_{s_j}, \mathbf{x}, \mathbf{x}_{r_i}) p_z(\mathbf{x}_{r_i}, \mathbf{x}) e^{i\omega \tau(\mathbf{x}_{s_j}, \mathbf{x}, \mathbf{x}_{r_i})} d\mathbf{x}_{r_i}, \quad (14)$$

where

$$\tau(\mathbf{x}_{s_j}, \mathbf{x}, \mathbf{x}_{r_i}) = \tau(\mathbf{x}_{s_j}, \mathbf{x}) + \tau(\mathbf{x}, \mathbf{x}_{r_i}) \quad (15)$$

is the image condition given by the sum of the travel times of the path from the source station to the spreading point in subsurface  $\tau(\mathbf{x}_{s_j}, \mathbf{x})$  and from the spreading point to the receiver station  $\tau(\mathbf{x}, \mathbf{x}_{r_i})$ . The two paths are represented in Figure 8 by the red and blue lines respectively.

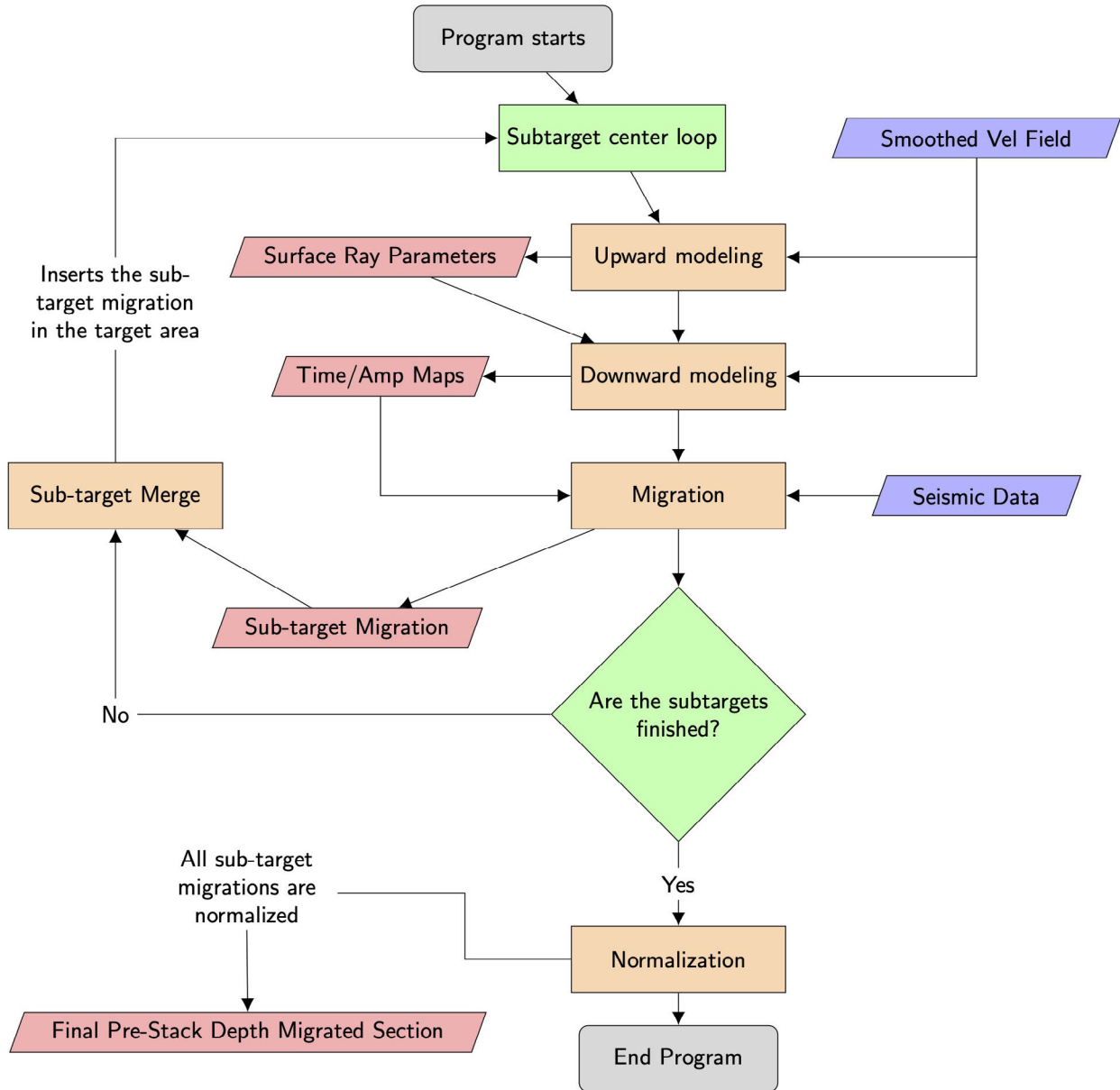


Figure 3. Diagram with the main steps of the target-oriented approach, with the input (blue parallelogram) and output (red parallelogram) data used in the algorithm.

From Equation 12 and considering the ray trajectory from the source and receiver, we have

$$\mathcal{J}(\mathbf{x}_s, \mathbf{x}) = \mathcal{J}(\mathbf{x}_s, \mathbf{x}_0) + \frac{\partial}{\partial \mathbf{x}_0} \mathcal{J}(\mathbf{x}_s, \mathbf{x}_0) \cdot \delta \mathbf{x} + \mathcal{O}(\mathbf{x} - \mathbf{x}_0)^2$$

and

$$\mathcal{J}(\mathbf{x}_r, \mathbf{x}) = \mathcal{J}(\mathbf{x}_r, \mathbf{x}_0) + \frac{\partial}{\partial \mathbf{x}_0} \mathcal{J}(\mathbf{x}_r, \mathbf{x}_0) \cdot \delta \mathbf{x} + \mathcal{O}(\mathbf{x} - \mathbf{x}_0)^2.$$

The total amplitudes  $\mathcal{A}$ , used in the imaging process are given by

$$\mathcal{A}(\mathbf{x}, \mathbf{x}_{s_j}, \mathbf{x}_{r_i}) = \frac{1}{\sqrt{\mathcal{J}(\mathbf{x}_{s_j}, \mathbf{x}) \mathcal{J}(\mathbf{x}_{r_i}, \mathbf{x})}}. \quad (16)$$

By reciprocity, we can assume that the travel time of the path represented by the black line is equal to the

blue line trajectory in Figure 8. Considering only the temporal part of Equation 14,

$$\hat{S}(\mathbf{x}_{s_j}, \mathbf{x}_{r_i}, t - \tau(\mathbf{x}_{s_j}, \mathbf{x}, \mathbf{x}_{r_i})) = \frac{\text{Re}}{\pi} \int_{\omega=0}^{+\infty} i\omega \Psi_0(\omega) S(\mathbf{x}_{s_j}, \mathbf{x}_r, \omega) e^{-i\omega[t - \tau(\mathbf{x}_{s_j}, \mathbf{x}, \mathbf{x}_{r_i})]} d\omega, \quad (17)$$

where  $\hat{S}$  represents the filtered seismic trace related to the shot at position  $\mathbf{x}_{s_j}$  and the receiver  $\mathbf{x}_{r_i}$  in the exact time  $\tau(\mathbf{x}_{s_j}, \mathbf{x}, \mathbf{x}_{r_i})$  equivalent to the trajectory between source  $\mathbf{x}_{s_j}$  and receiver  $\mathbf{x}_{r_i}$  to the diffracting point  $\mathbf{x}$ .

Replacing Equation 17 in 14, we have the operator that allows us to carry out the migration in the space

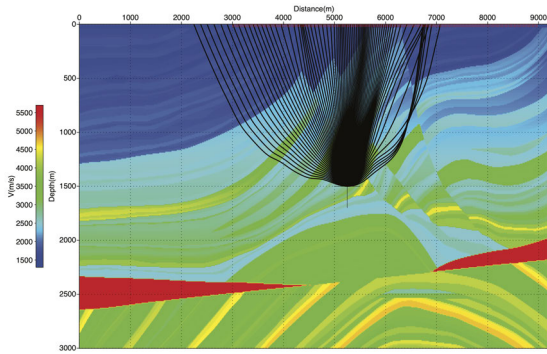


Figure 4. The first step of the modeling process. Rays are shot from the center of the target to the surface. The amplitude recorded on the surface estimates the illumination function of the sub-targets. This amplitude was used to determine which stations (sources and receivers) will contribute to the imaging of the sub-target.

domain, namely

$$u(\mathbf{x}, \mathbf{x}_{s_j}) = \int_{\mathbf{x}_{r_i} \in \Sigma_0} \mathcal{A}(\mathbf{x}, \mathbf{x}_{s_j}, \mathbf{x}_{r_i}) p_z(\mathbf{x}_{r_i}, \mathbf{x}) \hat{S}(\mathbf{x}_{s_j}, \mathbf{x}_{r_i}, t - \tau(\mathbf{x}, \mathbf{x}_{s_j}, \mathbf{x}_{r_i})) d\mathbf{x}_{r_i}. \quad (18)$$

The integral of Equation 18 is converted to a sum by

$$u(\mathbf{x}, \mathbf{x}_{s_j}) = \sum_{\mathbf{x}_{r_i} \in \Sigma_0} \Delta \mathbf{x}_{r_i} \mathcal{A}_{ij}(\mathbf{x}) p_z(\mathbf{x}_{r_i}, \mathbf{x}) \hat{S}(\mathbf{x}_{s_j}, \mathbf{x}_{r_i}, t - \tau_{ij}(\mathbf{x})), \quad (19)$$

where

$$\mathcal{A}_{ij}(\mathbf{x}) = \mathcal{A}(\mathbf{x}, \mathbf{x}_{s_j}, \mathbf{x}_{r_i}) \quad (20)$$

and

$$\tau_{ij}(\mathbf{x}) = \tau(\mathbf{x}, \mathbf{x}_{s_j}, \mathbf{x}_{r_i}). \quad (21)$$

The paraxial information is extrapolated from the central ray using Equations 15 and 16.

For each point  $\mathbf{x}$  in the sub-target area, we generate travel time and amplitude 2D maps  $(x, z)$  (Fig. 7) for all stations that will contribute to the target migration. Then, we sum the time of the propagated wavefield from the source  $\mathbf{x}_{s_j}$  and receiver  $\mathbf{x}_{r_i}$  stations to the point  $\mathbf{x}$ , as expressed in Eq. (21). Doing the same for the amplitudes, in Eq. (20), we have a time  $\tau_{ij}(\mathbf{x})$  and an amplitude  $\mathcal{A}_{ij}(\mathbf{x})$  function map for the source/receiver pair. With these function maps calculated, we can perform the depth migration of the seismic data at point  $\mathbf{x}$  by the equation:

$$u(\mathbf{x}) = \sum_{\mathbf{x}_{s_j}} \sum_{\mathbf{x}_{r_i} \in \Sigma_0} \Delta \mathbf{x}_{s_j} \Delta \mathbf{x}_{r_i} \mathcal{A}_{ij}(\mathbf{x}) p_z(\mathbf{x}_{r_i}, \mathbf{x}) \hat{S}(\mathbf{x}_{s_j}, \mathbf{x}_{r_i}, t - \tau_{ij}(\mathbf{x})). \quad (22)$$

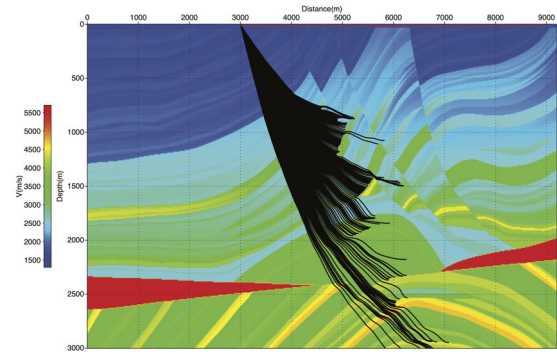


Figure 5. In the second step of the modeling process, rays are traced from the station on the surface, with an angular variation that corresponds to the position of the sub-target in depth. With increasing depth and seismic velocity, the rays curve upwards (turning rays). To avoid the low illumination of the target area, the width of the sub-targets must be a few hundred meters. The propagation of the rays was stopped the instant they became ascending.

The final image is computed by

$$I(\mathbf{x}) = \frac{u(\mathbf{x})}{\sum_{\mathbf{x}_{s_j}} \sum_{\mathbf{x}_{r_i} \in \Sigma_0} \Delta \mathbf{x}_{s_j} \Delta \mathbf{x}_{r_i} \mathcal{A}_{ij}(\mathbf{x})}. \quad (23)$$

We apply the ray tracing migration to Marmousoft synthetic seismic data (Billette *et al.*, 2003). The result of target-oriented migration  $I(\mathbf{x})$  in the Marmousoft model using Equation 23 can be seen in Figure 9 and, in a more detailed manner in Figure 10. The target area at coordinates  $x$  5500m to 7500m and  $z$  0m to 2000m was divided in 8 sub-targets with 1000 meters and 500 meters of vertical and horizontal length, respectively. The final grid of the migrated sections has a 10 meter both vertical and horizontal spacing interval.

The plots are generated with the Seismic Unix package (Stockwell and Cohen, 1995), with an amplitude gain of `perc=99.0`. No image received any treatment or filtering, being a direct result of the target-oriented migration algorithm (Fig. 15a). The respective true interval velocity of the Marmousoft model is placed next to each seismic section for comparison purposes, as shown in Figure 15b.

### The vector amplitude

During this work we link the slowness vectors  $\mathbf{p}_{r_i}$  and  $\mathbf{p}_{s_j}$  (Fig. 11), related to source and receiver, with the amplitude values registered in the seismic data. But the ray parameter is determined only by the ray tracing propagator in Eq. (6), performed in the low-frequency portion of the seismic velocity field, and it has no relationship with the real seismic amplitudes.

By applying the vertical and horizontal components of the slowness vector during the seismic migration, we can produce an image for each component (Figs. 12

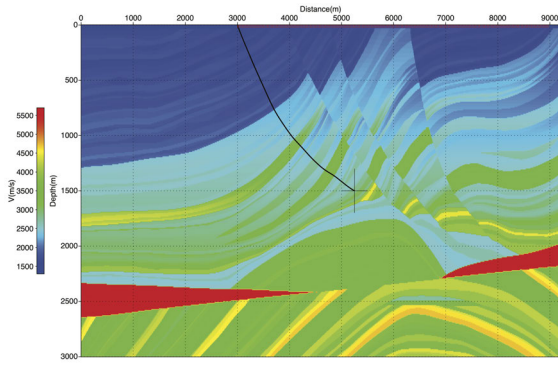


Figure 6. One ray traced on the Marmousi synthetic velocity model towards the center of the target in the second step of Figure 5. For each ray, the travel times, amplitudes (Fig. 7) and the vector slowness will be extrapolated. The velocity model used was smoothed with a 200m operator. The true velocity model was plotted for illustration purposes.

and 13), or combine them into a migration scheme, which we call the vector amplitude approach (Fig. 14b).

Let us consider a change in the migration amplitude of Eq. (20), where the amplitude  $A_{ij}$  became weighted by the angle of incidence at point  $x$ , according to the trajectory of each ray, such that

$$A_{ij_{px}}(x) = A_{ij}(x)(px_{s_j} + px_{r_i}), \quad (24)$$

and

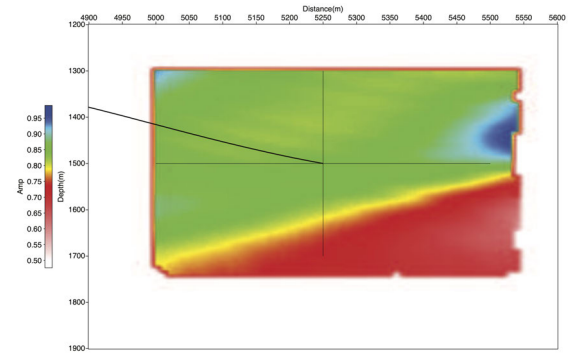
$$A_{ij_{pz}}(x) = A_{ij}(x)(pz_{s_j} + pz_{r_i}), \quad (25)$$

where  $px_{s_j}$ ,  $px_{r_i}$  are the horizontal components and  $pz_{s_j}$ ,  $pz_{r_i}$  are the vertical components of the slowness vector of the ray coming out of the source and receiver, respectively, towards point  $x$  (Fig. 8).

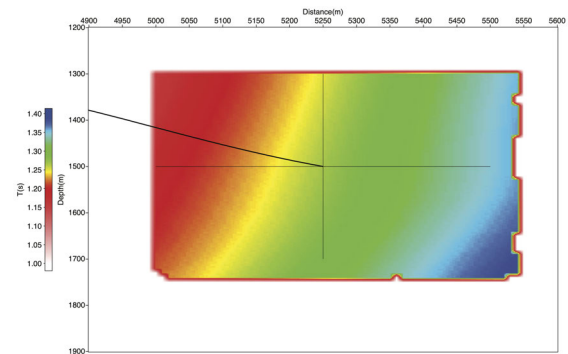
We can perform two separated migrations based on the amplitudes weighted by the vertical and horizontal components of the slowness vector. If we substitute the amplitudes  $A_{ij}$  in Eq. (22) by the amplitudes  $A_{ij_{px}}$  in Eq. (24), we obtain the horizontal component of the migrated section, presented in Figure 12. Doing the same for the vertical component of the slowness vector, we obtain the migrated section weighted by  $pz_{r_i} + pz_{s_j}$  (Fig. 13).

The migrated section, weighted by the horizontal components of the slowness vector (Fig. 12), shows several non-collapsed diffractions, while the migrated section in Figure 13 is almost the same like the ray tracing migration shown in Figure 10. We do not need to explicitly compute these two migrations. They are shown here to exemplify an intermediate process in the construction of vector amplitudes.

To perform the migration with vector amplitude, we could simply sum the squares of the migrations weighted by the slowness vector components, in a vector sum context. The slowness vector sum (Fig. 11) of source and receiver,  $ps_j + pr_i = ps_{j,r_i}$ , can be ex-



(a) Amplitudes



(b) Travel times

Figure 7. Amplitude (a) and travel time (b) maps referring to paraxial extrapolation of the central ray values. The cross, whose vertical line is 1000 meters long and the horizontal line is 500 meters long, corresponds to the sub-target and defines the area where the paraxial parameters will be extrapolated.

pressed in the component form by

$$|ps_{j,r_i}| = \sqrt{[(px_{s_j} + px_{r_i})^2 + (pz_{s_j} + pz_{r_i})^2]} \quad (26)$$

where  $ps_{j,r_i}$  is the result of the vector sum of the ray slowness, from the source and receiver towards point  $x$  in the grid (Fig. 8). By applying the concept of Eq. (26) we can reach a modified migration scheme, denoted by

$$I_v(x) = \text{sign}[I(x)] \frac{\sum_{\substack{\mathbf{x}_{s_j}, \mathbf{x}_{r_i} \in \Sigma_0 \\ \mathbf{x}_{s_j}, \mathbf{x}_{r_i} \in \Sigma_0}} \Delta \mathbf{x}_{s_j} \Delta \mathbf{x}_{r_i}}{\sum_{\substack{\mathbf{x}_{s_j}, \mathbf{x}_{r_i} \in \Sigma_0 \\ \mathbf{x}_{s_j}, \mathbf{x}_{r_i} \in \Sigma_0}} \Delta \mathbf{x}_{s_j} \Delta \mathbf{x}_{r_i}} \frac{\sqrt{[\hat{S}_{ij}(t - \tau_{ij}(x))A_{ij_{px}}(x)]^2 + [\hat{S}_{ij}(t - \tau_{ij}(x))A_{ij_{pz}}(x)]^2}}{\sqrt{[A_{ij_{px}}(x)]^2 + [A_{ij_{pz}}(x)]^2}} \quad (27)$$

where

$$\hat{S}_{ij}(t - \tau_{ij}(x)) = \hat{S}(\mathbf{x}_{s_j}, \mathbf{x}_{r_i}, t - \tau_{ij}(x)). \quad (28)$$

The result of migration with vector amplitudes  $I_v(x)$  is shown in Figure 14a and the true velocity model in Fig-

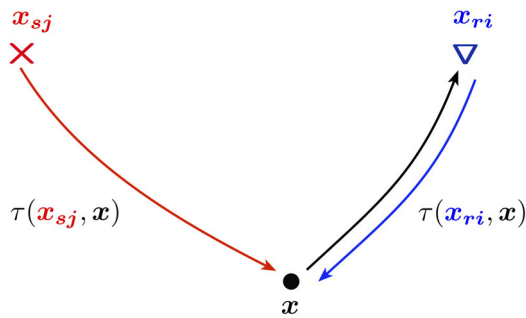


Figure 8. The imaging condition, for a source and a receiver, is the travel time sum of the path from the point to be imaged to the respective stations. The red ray represents the trajectory of the wave propagated from the source  $x_{sj}$  to the diffracting point  $x$ ; while the blue ray represents the trajectory from the receiver  $x_{ri}$  to the point  $x$  in subsurface.

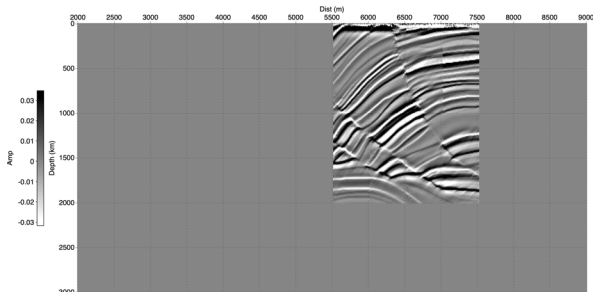


Figure 9. Target-oriented ray tracing migration at coordinates  $x$  5500m to 7500m and  $z$  0m to 2000m. Imaging is performed only in the pre-selected area.

ure 14b. It is possible to see that there is a good correlation between them. If we compare Figure 14b with Figure 10, we notice an increase in resolution in reflectors and faults. The vector amplitude acts as a filter, attenuating diffractions in regions of high velocity contrast.

We assume that the vector amplitude migration resulted in an improvement in the imaging of the synthetic seismic data of the Marmousi model. In this way, we present the results of the ray tracing migration with vector amplitudes applied to Marmousoft data. We performed the migration in the entire Marmousi model with 18 sub-targets. Each sub-target is 1.5km and 1.0km long, vertically and horizontally, respectively. The final grid of the migrated section is 10 meter in both  $x$  and  $z$  direction.

Overall, the reflectors have good continuity and their spatial position seems to be correct, due to the correlation of the migrated section with the real velocity model (Fig. 15b). The upper part of the migrated section (from 0 to 50 meters in depth) has spurious amplitudes due to the input seismic data, which are not related to the migration algorithm.

In order to verify the accuracy of the algorithm's resolution, we performed the migration in the portion of the

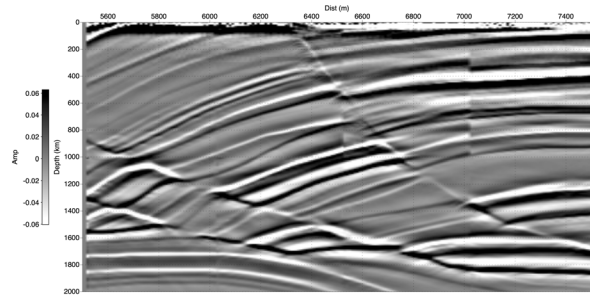


Figure 10. Detail of target-oriented ray tracing migration at coordinates  $x$  5500m to 7500m and  $z$  0m to 2000m.

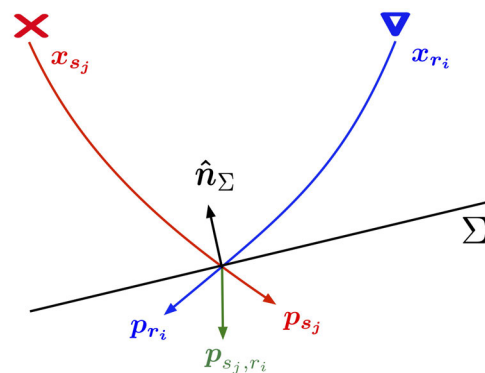


Figure 11. Schematic drawing of the slowness vectors  $p_{sj}$  and  $p_{ri}$ , associated to shot and receiver rays, respectively. They are the weights applied to the paraxial amplitude of the ray tracing to calculate the vector amplitude. The true reflector  $\Sigma$  and its normal  $\hat{n}_{\Sigma}$  are built as the imaging is performed and are always related to higher amplitudes of seismic data.

model with the lowest structural complexity. We defined the target region at coordinates  $x$  2500m to 4000m and  $z$  0m to 1500m. The area was divided into 6 sub-targets. Each sub-target is 500m long in the  $x$  direction and 750m in the  $z$  direction.

Figure 16 emphasizes the remarkable similarity between the stratigraphy of the geological layers in the migrated section and the true model. We observe that the resolution comes close to the interval velocity model. For instance, in Figure 16a, we can point out the channel structure (at a depth of 200 meters and coordinate  $x$  equal to 3100 meters) and the pinch-out (at a depth of 600 meters and coordinate  $x$  equal to 3700 meters).

The migrated section in Figure 17a aims to show the imaging result with the detail for the fault zone in the region of coordinates  $x$  3000m to 5000m and  $z$  0m to 1000m. The target-oriented approach in this migration used 4 sub-targets with 1000 meters of vertical length and 500 meters of horizontal length, for each sub-target. The marks of the borders between sub-targets #3 and #4 can be seen in Figure 17a. However, between sub-targets #1 and #2, the amplitudes



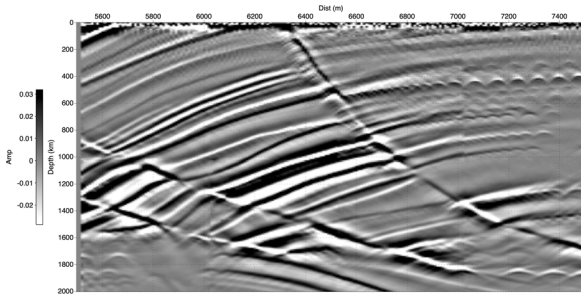


Figure 12. Detail of target-oriented ray tracing migration at coordinates  $x$  5500m to 7500m and  $z$  0m to 2000m with the amplitude weighted by the horizontal components of the slowness vector.

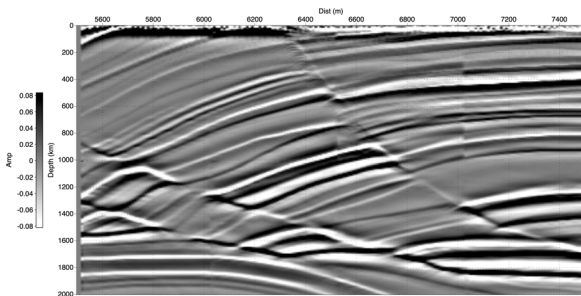


Figure 13. Detail of target-oriented ray tracing migration at coordinates  $x$  5500m to 7500m and  $z$  0m to 2000m with the amplitude weighted by the vertical components of the slowness vector.

were well equalized and the border vanishes.

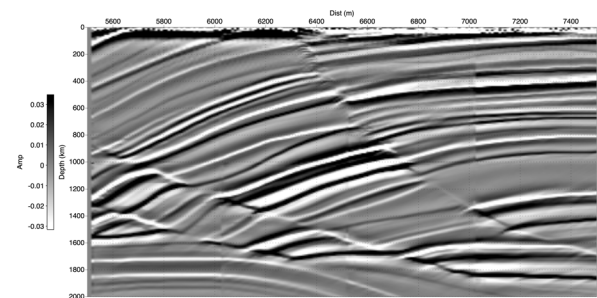
The fault region is well imaged and with little or no scattering and the horizons show good continuity. The boundaries of the sub-targets show differences in amplitude and frequency content, and sometimes some phase differences.

In regions of high structural complexity, these differences tend to be more expressive, as shown in Figure 14a. Due to the automatic choice of the input seismic traces that compose the migrated image, it is expected to have amplitude differences between the sub-targets since the migration of each sub-target is independent of the others.

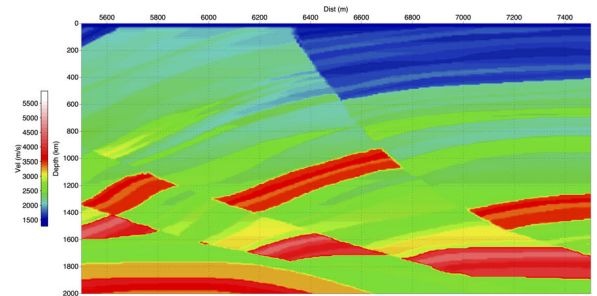
**The slowness vector image**

The subsequent strategy of linking the ray parameter with the seismic data consists of associating the *amplitudes as weights* for the components of the slowness vector. In this way, the amplitudes work as a probability distribution, where high amplitudes correspond to greater probabilities for a specific slowness vector to be present in the subsurface.

We do not know in advance the true reflector  $\Sigma$  (Fig. 11). However, we know that the highest amplitude values recorded in the seismogram are linked to this reflector, whose location has a relevant velocity contrast.

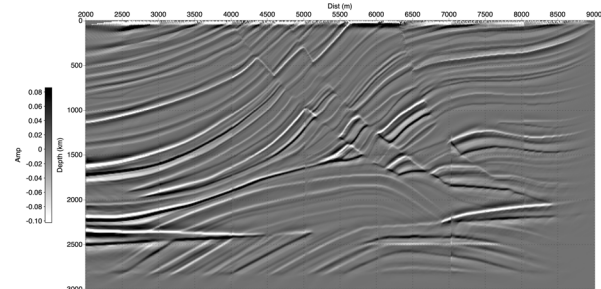


(a) Seismic section

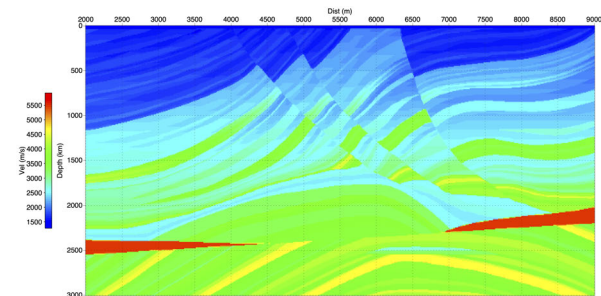


(b) Velocity

Figure 14. (a) Target-oriented ray tracing migration with vector amplitude, at coordinates  $x$  5500m to 7500m and  $z$  0m to 2000m. Note the general increase in resolution and continuity of the reflectors, as well as in geological faults, when compared with Figure 10. (b) True Marmousi velocity field at the same coordinates.

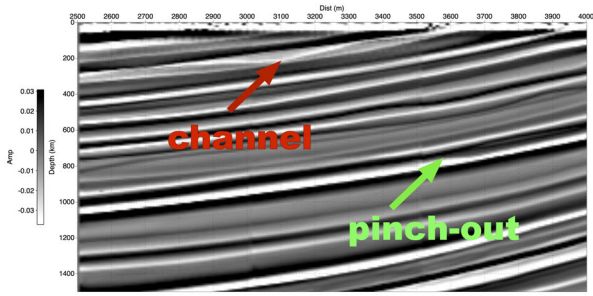


(a) Seismic section

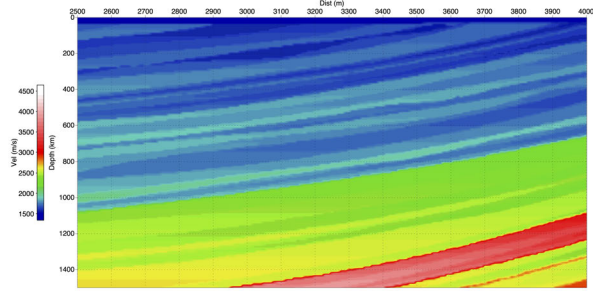


(b) Velocity

Figure 15. (a) Target-oriented ray tracing migration with vector amplitudes of Marmousi model. (b) Marmousi interval velocity field.



(a) Seismic section



(b) Velocity

Figure 16. (a) Target-oriented ray tracing migration with vector amplitudes at coordinates  $x$  2500m to 4000m and  $z$  0m to 1500m. Note the detail of the reflector resolution (channel and the pinch-out). (b) True Marmousi velocity field at the same coordinates. The maximum velocity was clipped at 4500m/s during the plot for better visualization.

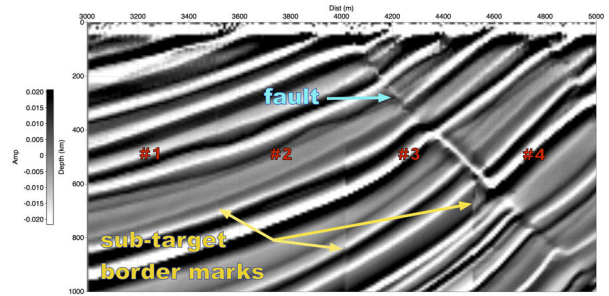
If there is a reflection at point  $\mathbf{x}$ , there must be a reflector such that the vector  $\mathbf{p}_{s_j, r_i}$  coincides with its normal  $\hat{\mathbf{n}}_\Sigma$ , as shown in Figure 11.

The constructive interference of many slowness vectors, weighted by their corresponding migration amplitudes, can define the normal vector to a probable reflector, as long as they are part of a source ( $\mathbf{p}_s$ ) and receiver ( $\mathbf{p}_r$ ) pair, whose image condition is associated with high amplitudes in the seismogram.

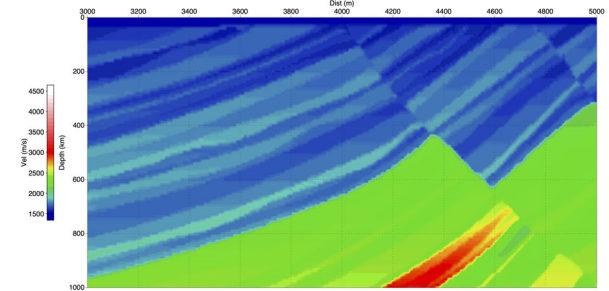
Following this idea, we can estimate the intensity  $I_n(\mathbf{x})$  in the direction of the vector  $\hat{\mathbf{n}}$ , normal to the probable reflector  $\Sigma$ . The sum of the slowness vector contributions, weighted by the amplitudes of the seismograms and normalized by the sum of the seismograms amplitudes, is given by

$$I_n(\mathbf{x}) = \frac{\sum_{\mathbf{x}_{s_j}, \mathbf{x}_{r_i} \in \Sigma_0} \Delta \mathbf{x}_{s_j} \Delta \mathbf{x}_{r_i}}{\sum_{\mathbf{x}_{s_j}, \mathbf{x}_{r_i} \in \Sigma_0} \Delta \mathbf{x}_{s_j} \Delta \mathbf{x}_{r_i}} \frac{\sqrt{[\hat{S}_{ji}(t - \tau_{ij}(\mathbf{x})) \mathcal{A}_{ij_{px}}(\mathbf{x})]^2 + [\hat{S}_{ji}(t - \tau_{ij}(\mathbf{x})) \mathcal{A}_{ij_{pz}}(\mathbf{x})]^2}}{\sqrt{[\hat{S}_{ji}(t - \tau_{ij}(\mathbf{x}))]^2 \mathcal{A}_{ij}(\mathbf{x})^2}} \quad (29)$$

All the ray migration equations are normalized by the



(a) Seismic section



(b) Velocity

Figure 17. (a) Target-oriented ray tracing migration with vector amplitudes at coordinates  $x$  3000m to 5000m and  $z$  0m to 1000m with detail to the fault. The numbers mark the centers of the sub-targets. Despite normalization efforts, some scars from imaging still resist at the borders of sub-targets. (b) True Marmousi velocity field at the same coordinates.

sum of the Jacobian amplitudes,  $\mathcal{A}_{ij}$  in Eq. (23), and  $\sqrt{(\mathcal{A}_{ij_{px}})^2 + (\mathcal{A}_{ij_{pz}})^2}$  in Eq. (27), as shown by the denominator of the aforementioned equations. It is done to guarantee that the final amplitudes of the migrated section are equalized and reliable to the seismic data values.

But in Eq. (29) we are normalizing by the seismic data themselves, weighted by the ray tracing amplitudes. In other words, we are removing the values related to the amplitude of the seismic traces and leaving only the module of the vectors normal to reflectors. The numerical result obtained from this scheme is shown in Figure 18. The slowness vector represents the direction of the ray, which is perpendicular to the wavefront. It is obtained from the ray tracing propagator and represents the properties of the velocity field used in the imaging. It has no relation to seismic data.

However, when we associate the highest amplitudes of the seismograms with these vectors, we can assume that they represent real subsurface attributes and not only parameters related to the velocity model and the propagator.

### CONCLUSION

In this study we performed the ray tracing migration with paraxial extrapolation of amplitudes and travel times ap-

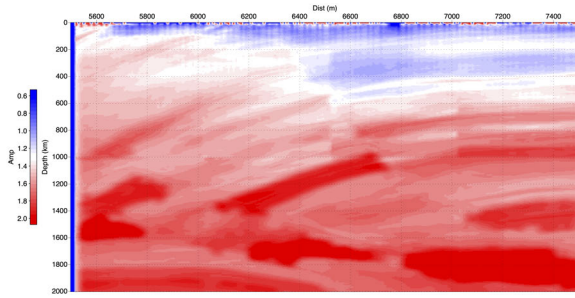


Figure 18. Slowness vector image. The amplitude values represent the module of the vector normal to true reflectors.

plied to the Marmousi model, whose result shows good correlation with the true velocity model. We demonstrated a target-oriented approach with automatic estimation of parameters, such as the aperture and angle of migration, which can potentially maximize the ray tracing migration speed, by selecting the traces that will compose the image.

Although this step (Fig. 4) reduced the amount of seismic traces used in the migration, it did not cause any loss of image quality. The automatic selection of the seismic data involved in the imaging avoids traces that do not contribute to the migration window, reducing scattering and increasing focus.

We used the slowness vector as a conditioner for migration amplitudes, generating what we call vector amplitudes. This procedure increased the resolution of horizons and faults, decreasing the spreading effect. The implementation of the migration algorithm is done in such a way that it makes natural and intuitive the migration of VSP (Vertical Seismic Profile) seismic data and land-based seismic data migration directly with topography.

Nevertheless, there is still room for improvement. We noticed that the sub-target boundaries have a mark due to amplitude and bandwidth differences. This effect is expected because each sub-target is a completely independent migration. Despite normalization efforts, the amplitude difference, characterized by the marks on the sub-target boundaries, still remains. These marks could interfere in the extraction of image attributes or other analysis before stacking such as AVO (Amplitude Versus Offset).

Finally, we introduced the slowness vector image as another seismic attribute. This image represents the intensity of a vector normal to reflectors associated with the highest seismic amplitudes which, in turn, represent the greatest velocity contrasts. We consider the slowness vector image to be a by-product of this overall imaging strategy. We will explore its meaning and use for seismic migration and velocity field inversion in a future work.

## APPENDIX A

### The target-oriented migration algorithm

---

#### Algorithm 1 Target-oriented migration algorithm

---

**Require:** Seismic data in shot domain; Depth interval velocity

**Ensure:** Pre-stack depth migrated seismic section

- 1: Read the input parameters
  - 2: Sub-target center ( $nc$ ) estimation
  - 3: **for**  $c \leftarrow 1$  to  $nc$  **do** ▷ sub-target loop
  - 4:     **procedure** MODELLING
  - 5:         From the sub-target center, shoot rays in every direction above, Figure 4, and store the ray amplitude  $a$  for all station ( $ns$ ) at surface level.
  - 6:         **for**  $s \leftarrow 1$  to  $ns$  **do** ▷ Shot loop
  - 7:             **if**  $a(s) \neq 0$  **then**
  - 8:                 From the shot station  $s$ , shoot the rays at the angle range that covers the sub-target, as shown in Figure 5, and store the amplitude, time travel and other ray parameters. Do the same for all receiver stations  $r \in s$ , whose amplitude is different from zero.
  - 9:             **end if**
  - 10:         **procedure** MIGRATION
  - 11:         **end procedure**
  - 12:     **end for**
  - 13:     **end procedure**
  - 14: **end for**
- 

## APPENDIX B

### Green's function derivative

The directional derivative of the asymptotic approximation of the Green's function, on the acquisition surface can be denoted by,

$$\begin{aligned}
 \frac{\partial}{\partial z(\mathbf{x}_{r_i})} G(\mathbf{x}, \mathbf{x}_{s_j}, \mathbf{x}_{r_i}, \omega) &\approx \Psi_0(\omega) A(\mathbf{x}_{s_i}, \mathbf{x}, \mathbf{x}_{r_i}) \\
 &\frac{\partial}{\partial z(\mathbf{x}_{r_i})} e^{i\omega [\tau(\mathbf{x}_{s_j}, x) + \tau(\mathbf{x}_{r_i}, x)]} \\
 &= i\omega \Psi_0(\omega) A(\mathbf{x}_{s_i}, \mathbf{x}, \mathbf{x}_{r_i}) \frac{\partial}{\partial z(\mathbf{x}_{r_i})} \tau(\mathbf{x}_{r_i}, x) \\
 &\quad e^{i\omega [\tau(\mathbf{x}_{s_j}, x) + \tau(\mathbf{x}_{r_i}, x)]} \\
 &= i\omega \Psi_0(\omega) A(\mathbf{x}_{s_i}, \mathbf{x}, \mathbf{x}_{r_i}) p_z(\mathbf{x}_{r_i}, x) \\
 &\quad e^{i\omega [\tau(\mathbf{x}_{s_j}, x) + \tau(\mathbf{x}_{r_i}, x)]}. \quad (30)
 \end{aligned}$$

Because the amplitude in Equation 16 is a smooth function in relation to  $\mathbf{x}_{r_i}$ , we can neglect its derivative.

APPENDIX C

The asymptotic amplitude

The chain rule for the rectangular coordinates gives

$$\frac{\partial}{\partial x} = \frac{\partial \sigma}{\partial x} \frac{\partial}{\partial \sigma} + \frac{\partial \alpha}{\partial x} \frac{\partial}{\partial \alpha}, \quad \frac{\partial}{\partial z} = \frac{\partial \sigma}{\partial z} \frac{\partial}{\partial \sigma} + \frac{\partial \alpha}{\partial z} \frac{\partial}{\partial \alpha}. \quad (31)$$

Applying Eq.(31) to the Jacobean of Eq.(3)

$$\frac{\partial \mathcal{J}}{\partial x} = \frac{\partial \sigma}{\partial x} \frac{\partial}{\partial \sigma} [[\mathbf{p}_\sigma, \mathbf{p}_\alpha]] + \frac{\partial \alpha}{\partial x} \frac{\partial}{\partial \alpha} [[\mathbf{p}_\sigma, \mathbf{p}_\alpha]] \quad (32)$$

$$\frac{\partial \mathcal{J}}{\partial z} = \frac{\partial \sigma}{\partial z} \frac{\partial}{\partial \sigma} [[\mathbf{p}_\sigma, \mathbf{p}_\alpha]] + \frac{\partial \alpha}{\partial z} \frac{\partial}{\partial \alpha} [[\mathbf{p}_\sigma, \mathbf{p}_\alpha]] \quad (33)$$

Assuming that  $\frac{\partial x}{\partial \alpha}$  and  $\frac{\partial z}{\partial \sigma}$  exist and are continuous, then we have

$$\frac{\partial}{\partial \alpha} \left( \frac{\partial \mathbf{x}}{\partial \sigma} \right) = \frac{\partial}{\partial \sigma} \left( \frac{\partial \mathbf{x}}{\partial \alpha} \right), \quad (34)$$

It follows

$$\frac{\partial^\sigma \mathcal{J}}{\partial x} = \frac{\partial \sigma}{\partial x} \left\{ \left[ \left[ \frac{\partial p_\sigma}{\partial \sigma}, p_\alpha \right] \right] + \left[ \left[ p_\sigma, \frac{\partial p_\sigma}{\partial \alpha} \right] \right] \right\} + \quad (35)$$

$$\frac{\partial \alpha}{\partial x} \left\{ \left[ \left[ \frac{\partial p_\sigma}{\partial \alpha}, p_\alpha \right] \right] + \left[ \left[ p_\sigma, \frac{\partial p_\alpha}{\partial \alpha} \right] \right] \right\}, \quad (36)$$

$$\frac{\partial^\sigma \mathcal{J}}{\partial z} = \frac{\partial \sigma}{\partial z} \left\{ \left[ \left[ \frac{\partial p_\sigma}{\partial \sigma}, p_\alpha \right] \right] + \left[ \left[ p_\sigma, \frac{\partial p_\sigma}{\partial \alpha} \right] \right] \right\} + \quad (37)$$

$$\frac{\partial \alpha}{\partial z} \left\{ \left[ \left[ \frac{\partial p_\sigma}{\partial \alpha}, p_\alpha \right] \right] + \left[ \left[ p_\sigma, \frac{\partial p_\alpha}{\partial \alpha} \right] \right] \right\}, \quad (38)$$

For a 2D homogeneous medium with  $\mathcal{J} = s = \frac{\sigma}{c}$ , and therefore nearby a point source,  $p_\sigma$  and  $\frac{\partial p_\alpha}{\partial \alpha}$  will be parallel to the ray and the last determinant  $\left[ \left[ p_\sigma, \frac{\partial p_\alpha}{\partial \alpha} \right] \right]$  will be null. Given the absence of term  $\frac{\partial p_\alpha}{\partial \alpha}$  in Eq. (7), we will assume the contribution of the latter determinant  $\left[ \left[ p_\sigma, \frac{\partial p_\alpha}{\partial \alpha} \right] \right]$  as negligible also for non-homogeneous media and will have

$$\frac{\partial \mathcal{J}}{\partial x} = \frac{\partial \sigma}{\partial x} \left\{ \frac{d_{p_\sigma x} dz}{d\sigma d\alpha} - \frac{d_{p_z z} dx}{d\sigma d\alpha} + \frac{d_{p_z z} dx}{d\alpha d\sigma} - \quad (39)$$

$$\frac{d_{\mathcal{F}_{\sigma x}} dz}{d\alpha d\sigma} \right\} + \frac{\partial \alpha}{\partial x} \left\{ \frac{d_{D_{\sigma x}} dz}{d\alpha d\alpha} - \frac{d_{p_\sigma z} dx}{d\alpha d\alpha} \right\}, \quad (40)$$

$$\frac{\partial \mathcal{J}}{\partial z} = \frac{\partial \sigma}{\partial z} \left\{ \frac{d_{p_\sigma x} dz}{d\sigma d\alpha} - \frac{d_{p_z z} dx}{d\sigma d\alpha} + \frac{d_{D_z} dx}{d\alpha d\sigma} - \quad (41)$$

$$\frac{d_{p_\sigma x} dz}{d\alpha d\sigma} \right\} + \frac{\partial \alpha}{\partial z} \left\{ \frac{d_{p_\sigma x} dz}{d\alpha d\alpha} - \frac{d_{p_\sigma z} dx}{d\alpha d\alpha} \right\}. \quad (42)$$

All terms of these equations are available in the kinematic (6) or dynamic (7) systems except for terms  $\frac{\partial \sigma}{\partial x}, \frac{\partial \theta}{\partial x}, \frac{\partial \sigma}{\partial z}, \frac{\partial \theta}{\partial z}$  that can be determined by the inverse of matrix  $\left[ \frac{dx}{d\gamma} \right]$ .

REFERENCES

Baysal, E.; Kosloff, D.D.; Sherwood, J.W.C. Reverse Time Migration. *GEOPHYSICS* **1983**, *48*, 1514–1524. [10.1190/1.1441434](https://doi.org/10.1190/1.1441434).

Billette, F.; Bégat, S.L.; Podvin, P.; Lambaré, G. Practical Aspects and Applications of 2D Stereotomography. *GEOPHYSICS* **2003**, *68*, 1008–1021. [10.1190/1.1581072](https://doi.org/10.1190/1.1581072).

Biondi, B.L. *3D Seismic Imaging*, 1st edition ed.; Society Of Exploration Geophysicists: Tulsa, Okla, 2006.

Bleistein, N.; Cohen, J.K.; Stockwell, J.W.J. *Mathematics of Multidimensional Seismic Imaging, Migration, and Inversion*, 2001st edition ed.; Springer: New York, 2000.

Bleistein, N. *Mathematical Methods for Wave Phenomena*, 1st edition ed.; Academic Press: New York, 1984.

Carcione, J.M.; Herman, G.C.; ten Kroode, A.P.E. Seismic Modeling. *GEOPHYSICS* **2002**, *67*, 1304–1325. [10.1190/1.1500393](https://doi.org/10.1190/1.1500393).

Cerveny, V. *Seismic Ray Theory*, 1st edition ed.; Cambridge University Press: Cambridge, U.K. ; New York, 2001.

Chapman, C. *Fundamentals of Seismic Wave Propagation*; Cambridge University Press, 2004.

Cunha, P.E.M.; Mansur, W.J.; Universidade, F.d.R.d.J. Imageamento Sísmico Por Propagação de Ondas No Limite de Altas e Baixas Frequências. PhD thesis, UFRJ, Rio de Janeiro, 2005.

Cunha, P.E.M. A 2D Ray-Based Maximum Field Green’s Function Simulator. In *11th International Congress of the Brazilian Geophysical Society & EXPOGEF 2009, Salvador, Bahia, Brazil, 24-28 August 2009*; SEG Global Meeting Abstracts, Brazilian Geophysical Society, 2009; pp. 1594–1599. [10.1190/sbgf2009-336](https://doi.org/10.1190/sbgf2009-336).

Gajewski, D.; Coman, R.; Vanelle, C. Amplitude Preserving Kirchhoff Migration: A Traveltime Based Strategy. *Studia Geophysica et Geodaetica* **2002**, *46*, 193–211. [10.1023/A:1019849919186](https://doi.org/10.1023/A:1019849919186).

Gray, S.H. Gaussian Beam Migration of Common-Shot Records. *GEOPHYSICS* **2005**, *70*, S71–S77. [10.1190/1.1988186](https://doi.org/10.1190/1.1988186).

Hertweck, T.; Jäger, C.; Goertz, A.; Schleicher, J. Aperture Effects in 2.5D Kirchhoff Migration: A Geometrical Explanation. *GEOPHYSICS* **2003**, *68*, 1673–1684. [10.1190/1.1620641](https://doi.org/10.1190/1.1620641).

Hill, N.R. Prestack Gaussian-beam Depth Migration. *GEOPHYSICS* **2001**, *66*, 1240–1250. [10.1190/1.1487071](https://doi.org/10.1190/1.1487071).

Klokov, A.; Fomel, S. Selecting an Optimal Aperture in Kirchhoff Migration Using Dip-Angle Images. *GEOPHYSICS* **2013**, *78*, S243–S254. [10.1190/geo2013-0109.1](https://doi.org/10.1190/geo2013-0109.1).

Koren, Z.; Xu, S.; Kosloff, D. Targeted Oriented

- Common Reflection Angle Migration. In *SEG Technical Program Expanded Abstracts 2002*; SEG Technical Program Expanded Abstracts, Society of Exploration Geophysicists, 2002; pp. 1196–1199. [10.1190/1.1816865](https://doi.org/10.1190/1.1816865).
- Operto, M.S.; Xu, S.; Lambaré, G. Can We Quantitatively Image Complex Structures with Rays? *GEOPHYSICS* **2000**, *65*, 1223–1238. [10.1190/1.1444814](https://doi.org/10.1190/1.1444814).
- Popov, M.M.; Semtchenok, N.M.; Popov, P.M.; Verdel, A.R. Depth Migration by the Gaussian Beam Summation Method. *GEOPHYSICS* **2010**, *75*, S81–S93. [10.1190/1.3361651](https://doi.org/10.1190/1.3361651).
- Popov, M.M. *Ray Theory and Gaussian Beam Method for Geophysics*; EDUFBA: Salvador, 2002.
- Rocha, D.; Sava, P.; Guitton, A. 3D Acoustic Least-Squares Reverse Time Migration Using the Energy Norm. *GEOPHYSICS* **2018**, *83*, S261–S270. [10.1190/geo2017-0466.1](https://doi.org/10.1190/geo2017-0466.1).
- Russell, B. A Simple Seismic Imaging Exercise. *The Leading Edge* **1998**, *17*, 885–889. [10.1190/1.1438059](https://doi.org/10.1190/1.1438059).
- Sava, P.; Fomel, S. Riemannian Wavefield Extrapolation. *Geophysics* **2005**, *70*, T45–T56. [10.1190/1.1925748](https://doi.org/10.1190/1.1925748).
- Schleicher, J.; Tygel, M.; Hubral, P. 3-D True-amplitude Finite-offset Migration. *GEOPHYSICS* **1993**, *58*, 1112–1126. [10.1190/1.1443495](https://doi.org/10.1190/1.1443495).
- Shragge, J.; Akerberg, P. Wave-Equation Migration in Generalized Coordinate Systems. *GEOPHYSICS* **2010**, *75*, Z79–Z80. [10.1190/1.3495581](https://doi.org/10.1190/1.3495581).
- Shragge, J.C. Riemannian Wavefield Extrapolation: Nonorthogonal Coordinate Systems. *GEOPHYSICS* **2008**, *73*, T11–T21. [10.1190/1.2834879](https://doi.org/10.1190/1.2834879).
- Stockwell, J.W.; Cohen, J.K., SU user's manual. In *Theory of Seismic Imaging*; Springer Berlin Heidelberg: Berlin, Heidelberg, 1995; pp. 217–258. [10.1007/BFb0012094](https://doi.org/10.1007/BFb0012094).
- Thierry, P.; Operto, S.; Lambaré, G. Fast 2-D ray+Born Migration/Inversion in Complex Media. *GEOPHYSICS* **1999**, *64*, 162–181. [10.1190/1.1444513](https://doi.org/10.1190/1.1444513).
- Versteeg, R. The Marmousi Experience: Velocity Model Determination on a Synthetic Complex Data Set. *The Leading Edge* **1994**, *13*, 927–936. [10.1190/1.1437051](https://doi.org/10.1190/1.1437051).
- Virieux, J.; Farra, V. Ray Tracing in 3-D Complex Isotropic Media: An Analysis of the Problem. *GEOPHYSICS* **1991**, *56*, 2057–2069. [10.1190/1.1443018](https://doi.org/10.1190/1.1443018).
- Virieux, J.; Operto, S. An Overview of Full-Waveform Inversion in Exploration Geophysics. *GEOPHYSICS* **2009**, *74*, WCC1–WCC26. [10.1190/1.3238367](https://doi.org/10.1190/1.3238367).
- Woodward, M.J.; Nichols, D.; Zdraveva, O.; Whitfield, P.; Johns, T. A Decade of Tomography. *GEOPHYSICS* **2008**, *73*, VE5–VE11. [10.1190/1.2969907](https://doi.org/10.1190/1.2969907).
- Zhou, H.W.; Hu, H.; Zou, Z.; Wo, Y.; Youn, O. Reverse Time Migration: A Prospect of Seismic Imaging Methodology. *Earth-Science Reviews* **2018**, *179*, 207–227. [10.1016/j.earscirev.2018.02.008](https://doi.org/10.1016/j.earscirev.2018.02.008).

**D.O.:** Conceptualization, Investigation, Methodology, Software, Writing – original draft, revising & editing; **L.G.:** Conceptualization, Methodology, Writing – original draft, revising & editing; **P.C.:** Conceptualization, Methodology, Software, Writing – original draft; **A.S.:** Methodology, Software, Writing – revising & editing.

Received on September 27, 2021/ Accepted on March 21, 2022.



-Creative Commons attribution-type BY